Supporting Information

Production of Methanol from Aqueous CO_2 by Using Co_3O_4 Nanostructures as Photocatalysts

Salvador Pocoví-Martínez,[1,] Inti Zumeta-Dube[1,2] and David Diaz[1,]**

1 Facultad de Química, Universidad Nacional Autónoma de México, Avenida Universidad 3000, Ciudad Universitaria, Coyoacán, CP 04510, México D. F. México

2 Current address: Centro de Investigación en Ciencia Aplicada y Tecnología Avanzada, Unidad Legaría, Instituto Politécnico Nacional. Calzada Legaria No. 694 Col. Irrigación, Del. Miguel Hidalgo, México D.F., C.P.:11500

Corresponding authors

*E-mail addresses: salvador.pocovi@hotmail.es; david@unam.mx.

Contents

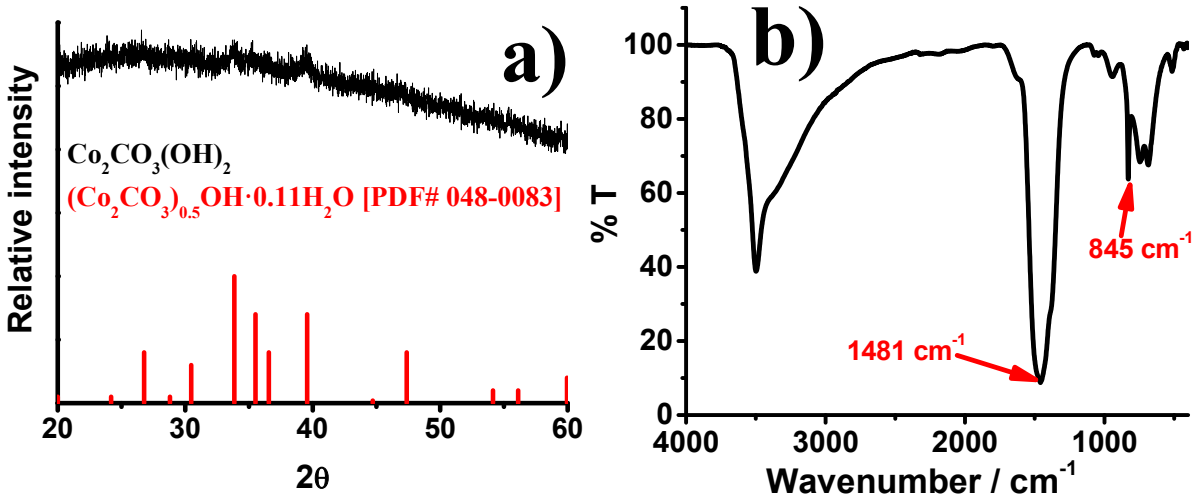

Fig. S1. a) PXRD pattern and b) IR spectrum of $CoCO_3(OH)_2$.

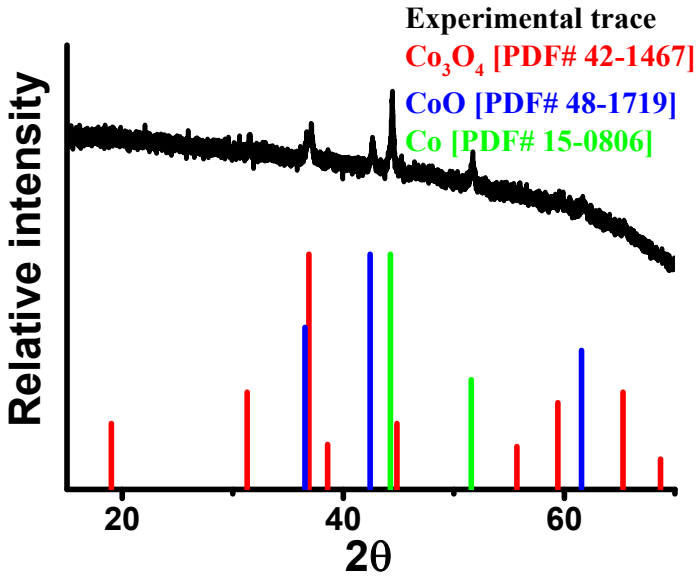

Fig. S2. PXRD pattern of the grey solid obtained in the synthesis of Co_3O_4-P-NS after combustion.

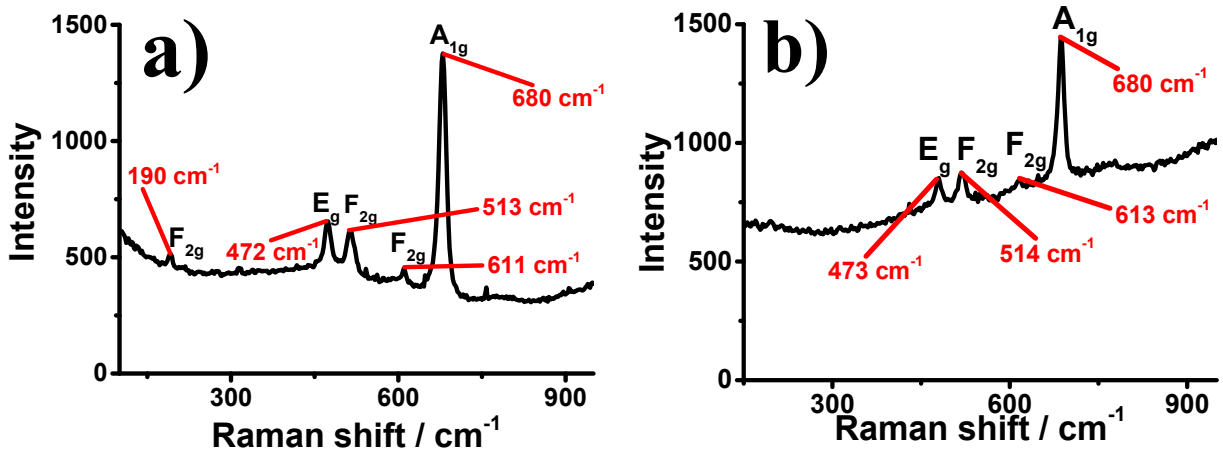

Fig. S3. Raman spectra recorded using a wavelength excitation laser source of 532 nm for a) Co_3O_4-NPs and b) Co_3O_4-P-NS.

As the Raman scattering spectroscopy is a powerful technique in structural materials characterization, it was used as a complement for phase identification of Co_3O_4 samples. Fig. S3a shows the Raman scattering spectrum of the Co_3O_4-NPs. The characteristic signals of this material are present in the spectrum profile as the unique detectable phase; that is in accordance with XRD results. The most intense signal appears at 680 cm^{-1}, it has been assigned to the A_{1g} mode [1,2]. For the Co_3O_4 spinel, this mode is attributed to the vibration of Co^{3+} in octahedral sites coordinated with oxygen atoms. The other four peaks at 191 cm^{-1} (F_{2g}), 472 cm^{-1} (A_{1g}), 513 cm^{-1} (F_{2g}) and 611 cm^{-1} (F_{2g}) are likely related to the combined vibrations of Co^{2+} in tetrahedral sites and octahedral oxygen motions [3]. In Fig. S3b, the Raman spectrum of Co_3O_4-P-NS is displayed. The same characteristic bands corresponding to this material are also present in that spectrum.

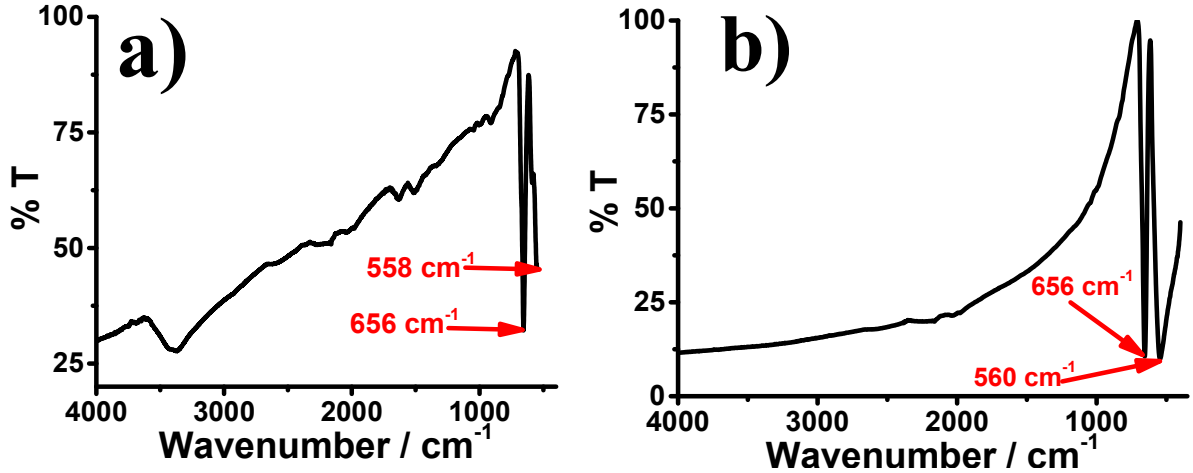

Fig. S4. IR spectra of a) Co_3O_4-NPs and b) Co_3O_4-P-NS.

Additionally, the IR spectra in Fig. S4a and Fig. S4b show two characteristic signals of this oxide, corresponding to the stretching vibration M-O: the band appearing at 656.46 cm^{-1} and 563.65 cm^{-1} attributed to the stretching of Co^{2+} in a tetrahedral hole and Co^{3+} in an octahedral hole, respectively [4,5].

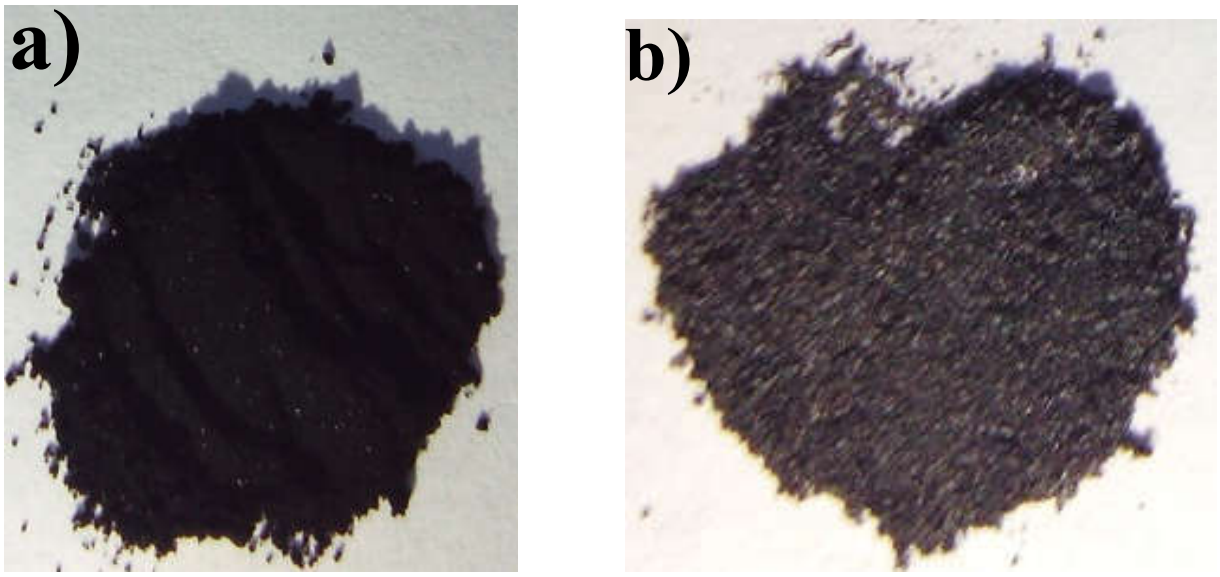

Fig. S5. Pictures of a) Co_3O_4-NPs and b) Co_3O_4-P-NS powders.

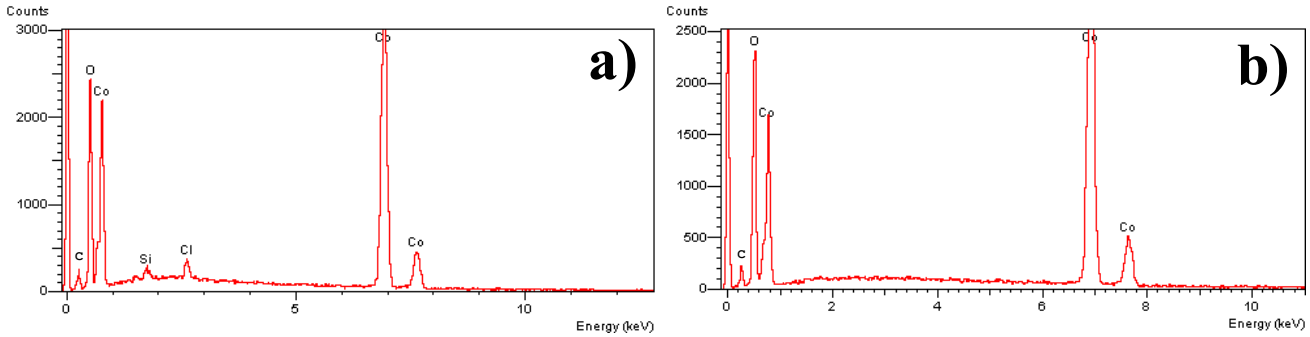

Fig. S6. EDS spectra of a) Co_3O_4-NPs and b) Co_3O_4-P-NS.

The EDS spectrum of Co_3O_4-NPs (Fig. S6a) displays the material composition. The very small chlorine quantity probably comes from the chlorinated precursor salt. Meanwhile the presence of the small remaining of Si can be due to some glass eroded, with the magnetic stirrer, of the reaction vessel, or as impurity in the Na_2CO_3 used in the synthesis reaction to form the $CoCO_3(OH)_2$. The EDS spectrum of Co_3O_4-P-NS (Fig. S6b) shows that this material does not present impurities by means of this technique. The presence of the small quantity of carbon in the two spectra can be due to CO_2 adsorbed on the surface of the materials; we

cannot discard the presence of a small amount of hydroxycarbonate for Co_3O_4-NPs and organic matter not removed for Co_3O_4-P-NS.

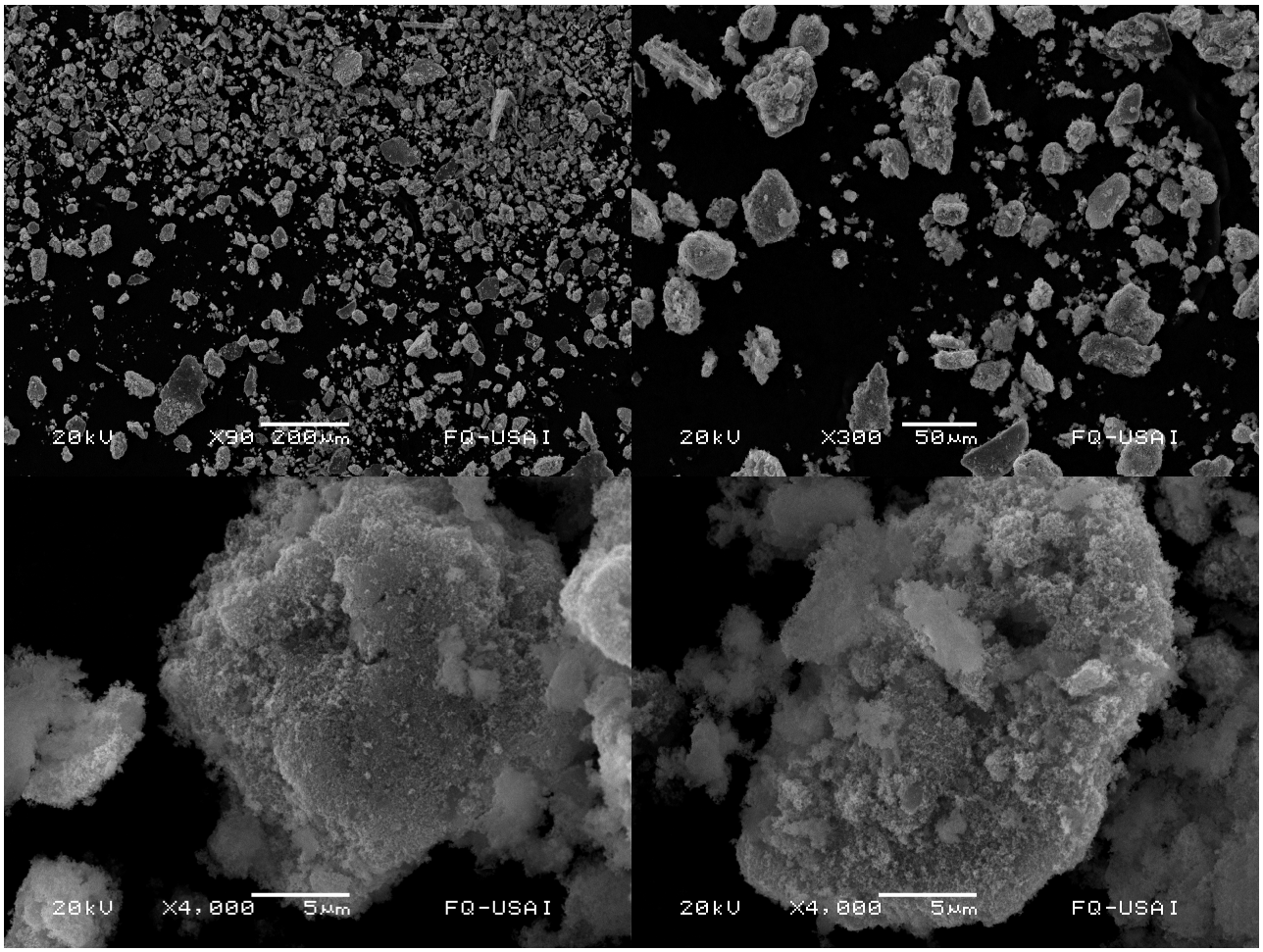

Fig S7. SEM images of Co_3O_4-NPs.

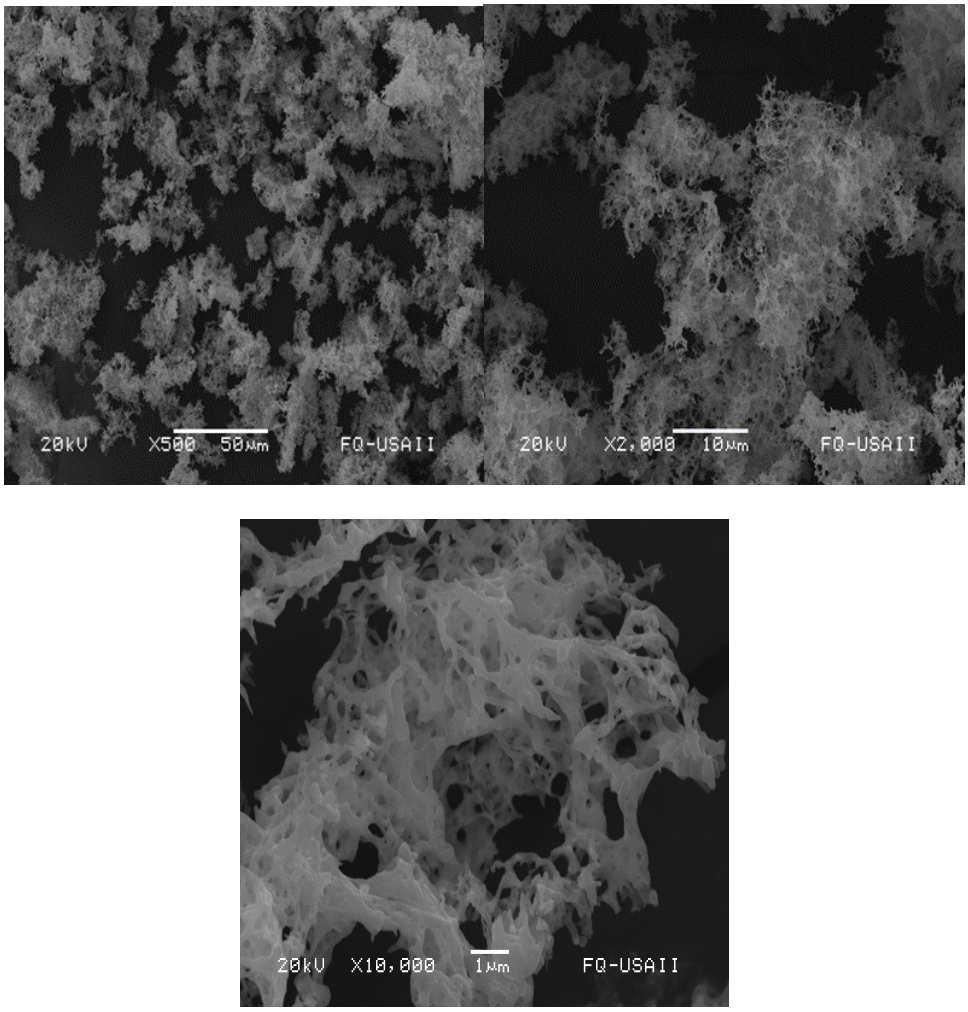

Fig S8. SEM images of Co_3O_4-P-NPs.

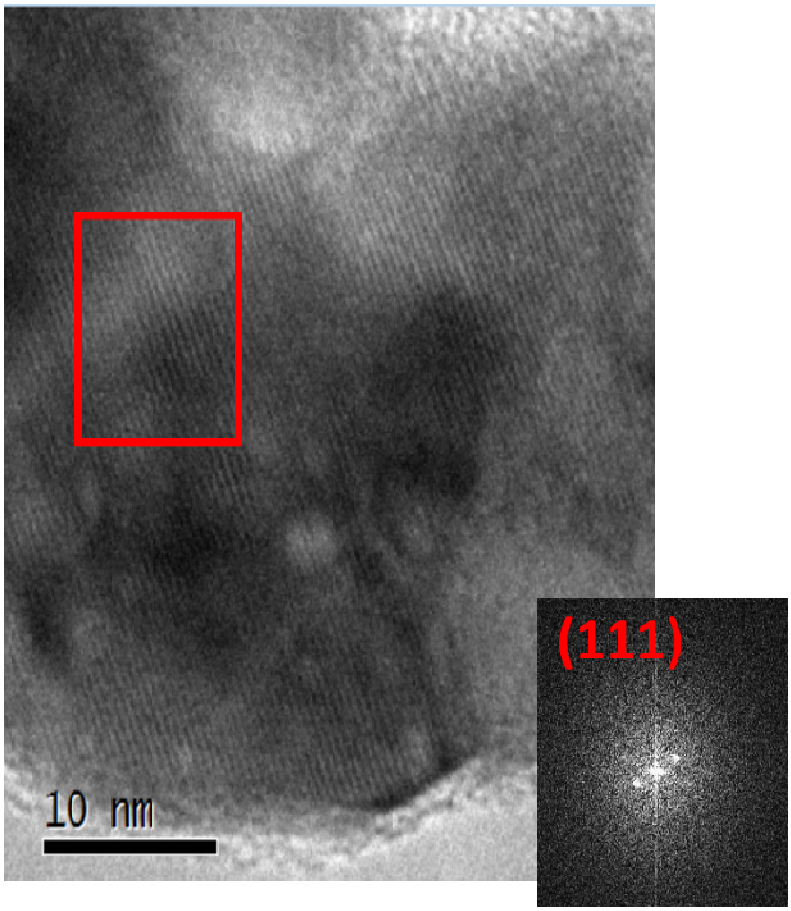

Fig S9. HRTEM image of Co_3O_4-P-NPs.

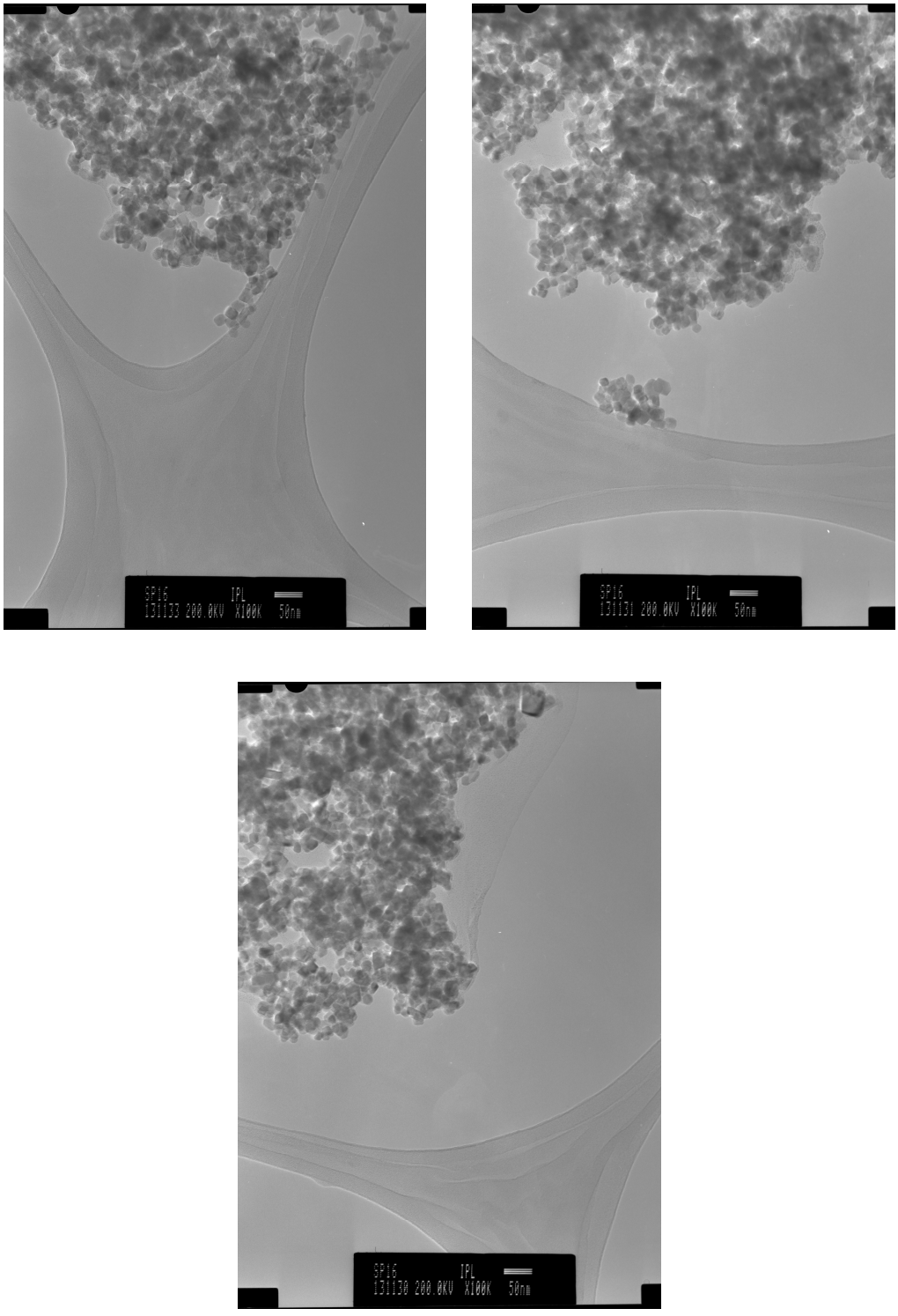

Fig S10. TEM images of Co_3O_4-NPs.

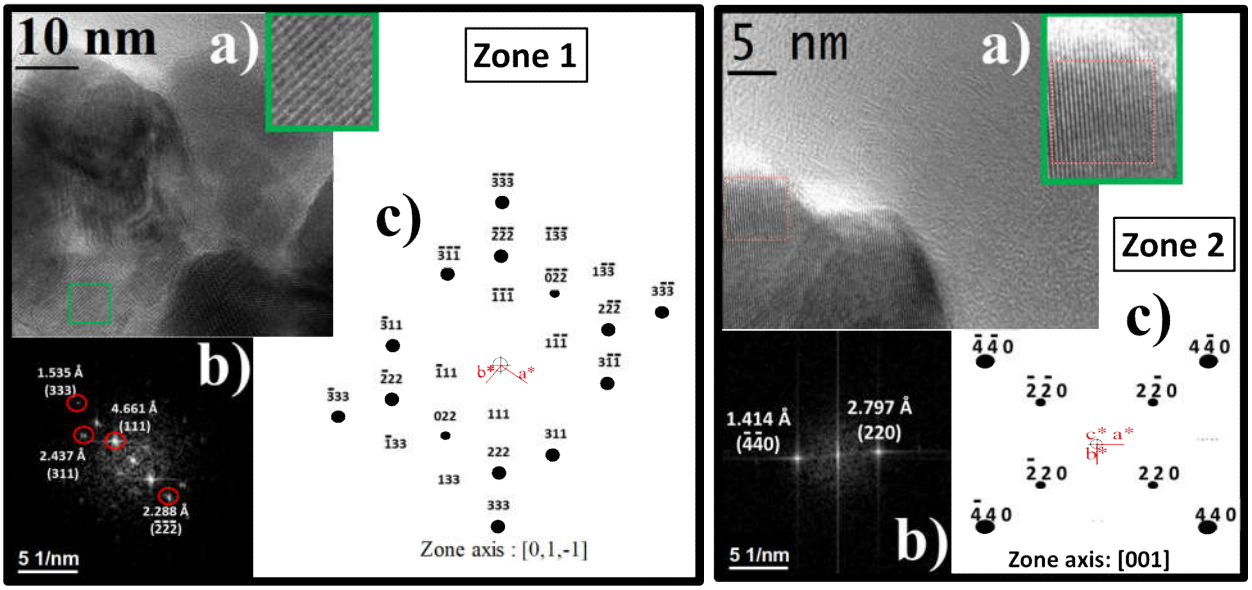

Fig S11. a) HR-TEM, b) FFT of the framed region and c) reciprocal lattice of 2 different zones of Co_3O_4-NPs.

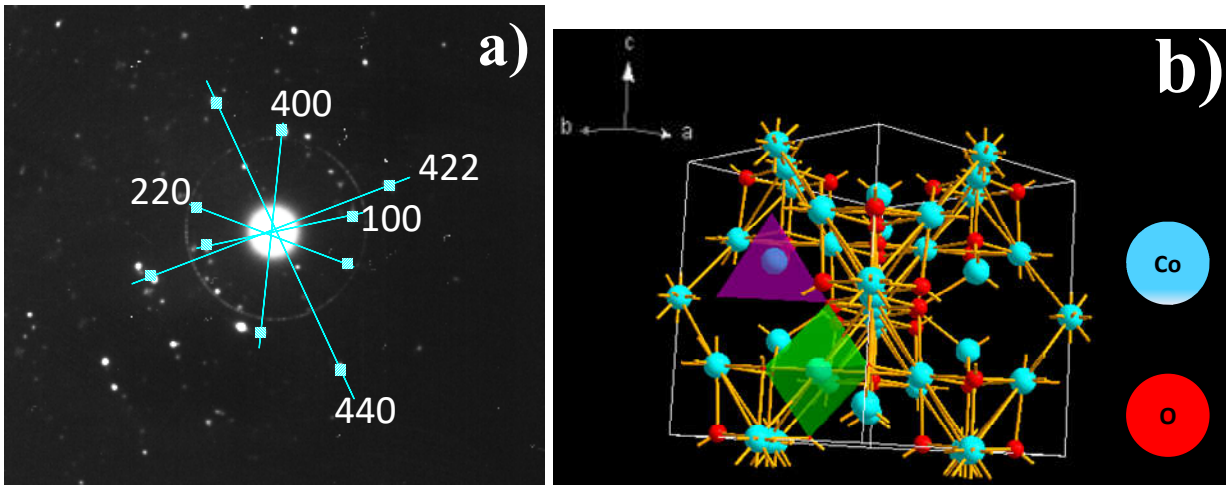

Fig. S12. a) SAED pattern and b) unit cell representation of Co_3O_4-NPs.

With the HR-TEM micrograph (Fig. S10a) the planes of the nanoparticles are observed and the calculated FFT, displayed in Fig. S7b for the green framed zone, gave different planes of Co_3O_4. The reciprocal lattice of this material, along the zone axis [0,1,-1], was also calculated (Fig. S10c). This could be corroborated in the SAED pattern in Fig. S8a. In Fig. S8b a representation of the unit cell is shown with the Co^{2+} in tetrahedral coordination (purple) and the Co^{3+} in octahedral coordination (green).

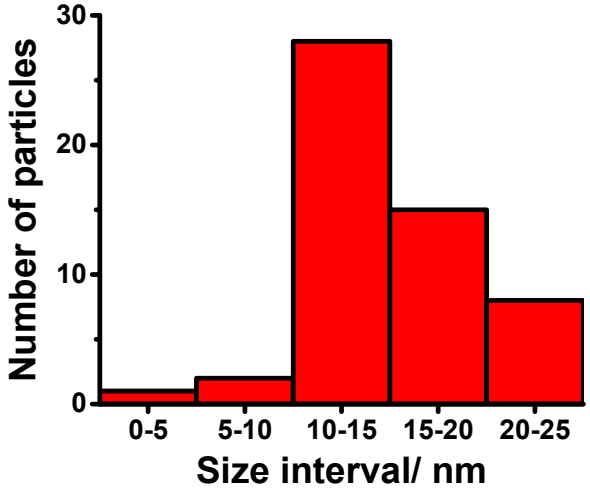

Fig. S13. Size distribution of Co_3O_4-NPs.

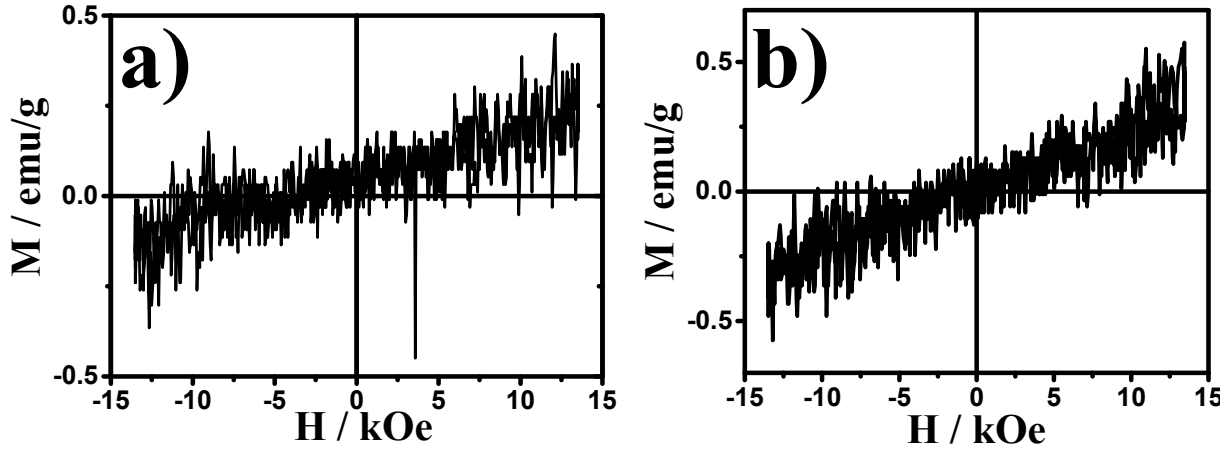

Fig. S14. Magnetization curves of a) Co_3O_4-NPs and b) Co_3O_4-P-NS.

As can be observed, the nanoparticles show an antiferromagnetic behavior at room temperature. It is well known that bulk Co_3O_4 and nanoparticles larger than 20 nm have this behavior too [6-10]. As an antiferromagnetic material, the Co_3O_4-NPs show a certain degree of ferromagnetism under the external magnetic field. One possible explanation for this is the unpaired atom spins orientation near the surface of the nanocrystals and a second may be the interaction between atoms [11].

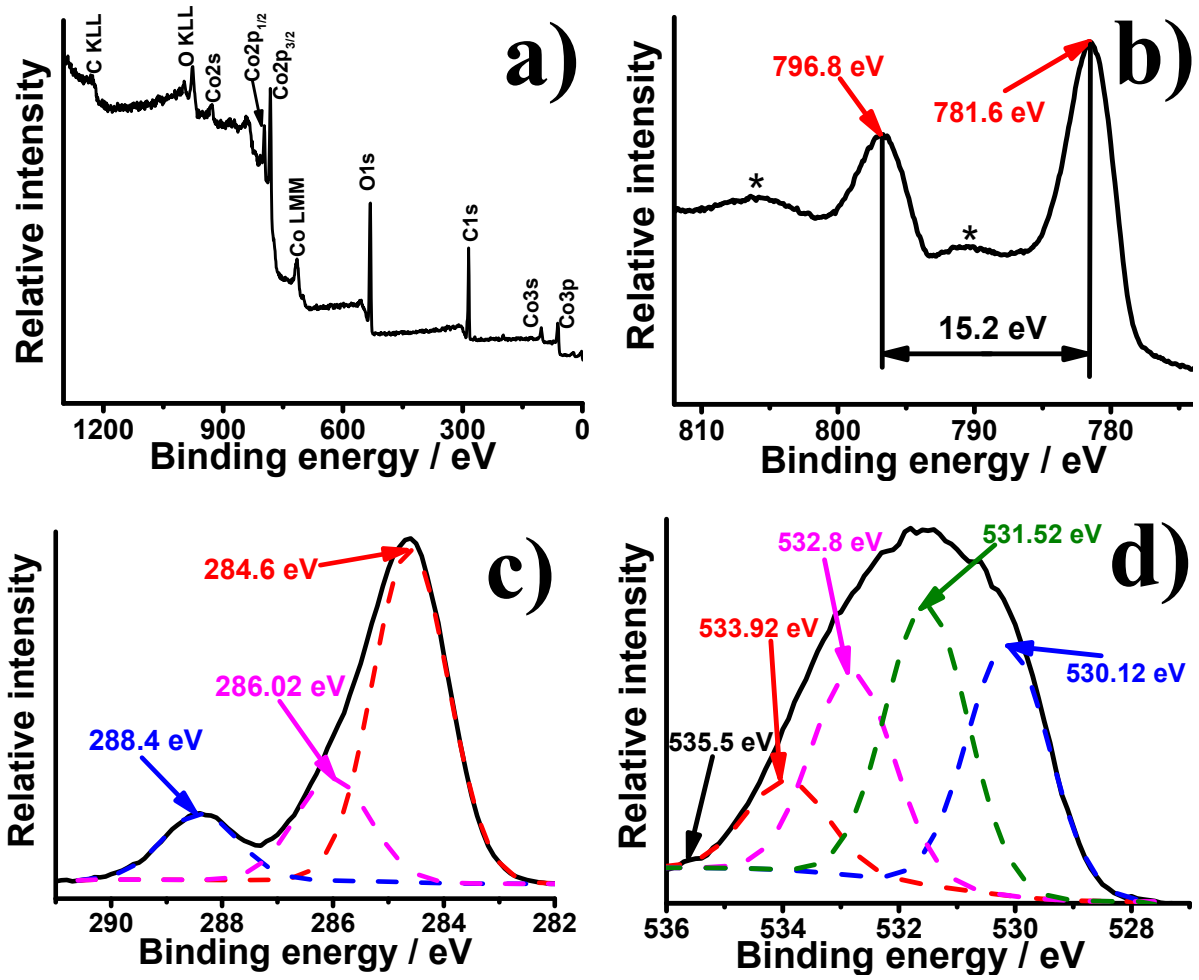

Fig. S15. XPS of Co_3O_4-NPs: a) wide range spectrum and high resolution spectra of b) Co2p, c) C1s and d) O1s.

It can be observed in the wide range spectrum (Fig. S14a) the peaks of Co2s, Co2p, Co3s, Co3p, O1s, and C1s as reported in literature [12-14]. The signals of $Co2p_{1/2}$ and $Co2p_{3/2}$ showed in the high resolution spectrum (Fig. S14b) are at 781.6 and 796.8 eV, respectively. The separation between these two signals is 15.2 eV [12,13, 15-17]. Two characteristic satellites (marked with *) of Co_3O_4 can be observed too [18-20]. In the high resolution spectrum of C1s (Fig. S14c) the experimental signal was deconvoluted into three different signals: 284.6 eV can be attributed to the adventitious hydrocarbons [21], 286.02 eV may be assigned to CO [14], and the signal at 288.4 eV can be attributed to the presence of CO_3^{2-} derived of the absorption of atmospheric CO_2 [19]. Finally, the signal of O1s (Fig. S14d) can be deconvoluted into four signals: 530.12 eV attributed to the lattice oxygen [17-19,22,23], 531.52 eV can be attributed to low coordinated oxygen species, OH^- or CO_3^{2-} on the surface of the material [17-19,21,23], 532.8 can be

assigned to O_2, H_2O, CO_3^{2-} or OH^- [19,21], and 533.92 eV may be attributed to the oxygen of water adsorbed on the surface [21]. Finally, a very weak peak at 535.5 eV is attributed to the lower binding energy shoulder of the Co Auger ($L_2M_{23}V$) transition [18]. It is difficult to assign the signals to one species since there can be inaccuracies in the peak fitting to report the true form of the peak or may be due to secondary electron background. Another problem that can appear in the assignment of the peaks is that the full width at half maximum of the deconvoluted peaks is around 2 eV, while for signals of single elements it is around 1.2 eV [18].

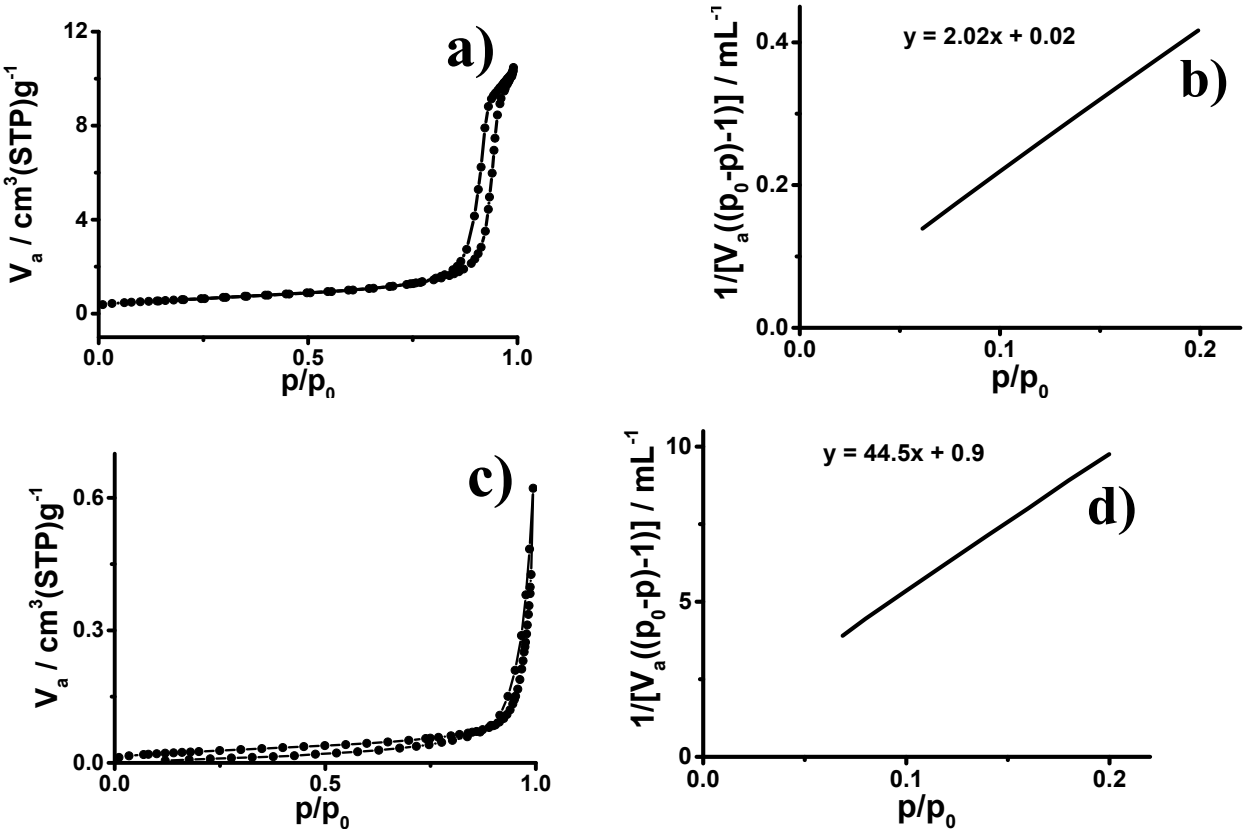

Fig. S16. Isotherm plot for adsorption-desorption of a) Co_3O_4-NPs and c) Co_3O_4-P-NS; BET surface area plot of b) Co_3O_4-NPs and d) Co_3O_4-P-NS.

In the pore size analysis (BET) for Co_3O_4-NPs, the isotherm for adsorption-desorption of N_2 gives a type IV plot (Fig. S15a), according to the Brunauer Deming Deming Teller classi cation; these results signi cantly indicate that the agglomerated nanoparticle structures are mesoporous. In addition, the Co_3O_4-NPs had well-de ned H3 sorption hysteresis loops. These results indicate that the shapes of mesopores are

slit-like [24]. The surface area of this material calculated from the nitrogen adsorption isotherm (Fig. S15b) is 48.0 m^2/g. In the BET experiment for Co_3O_4-P-NS, the isotherm for adsorption-desorption of N_2 gives a plot (Fig. S15c) with a type III shape, characterized by heats of adsorption lower than the adsorbate heat of liquefaction; adsorption proceeds as the adsorbate interaction with an adsorbed layer larger than the interaction with the adsorbent surface. The surface area for this material is 2.1 m^2/g, calculated from the nitrogen absorption isotherm (Fig. S15d). In this case, the size of the pores are in the order of microns (see Fig. 3c), though the existence of smaller pores is not excluded. The pores of the agglomerates of Co_3O_4-NPs have nanometric sizes (see Fig. 3a and Fig. 4 in the manuscript). Since the pores of Co_3O_4-NPs are smaller than the pores observed for Co_3O_4-P-NS, this could explain the great difference on the specific surface area of the two materials.

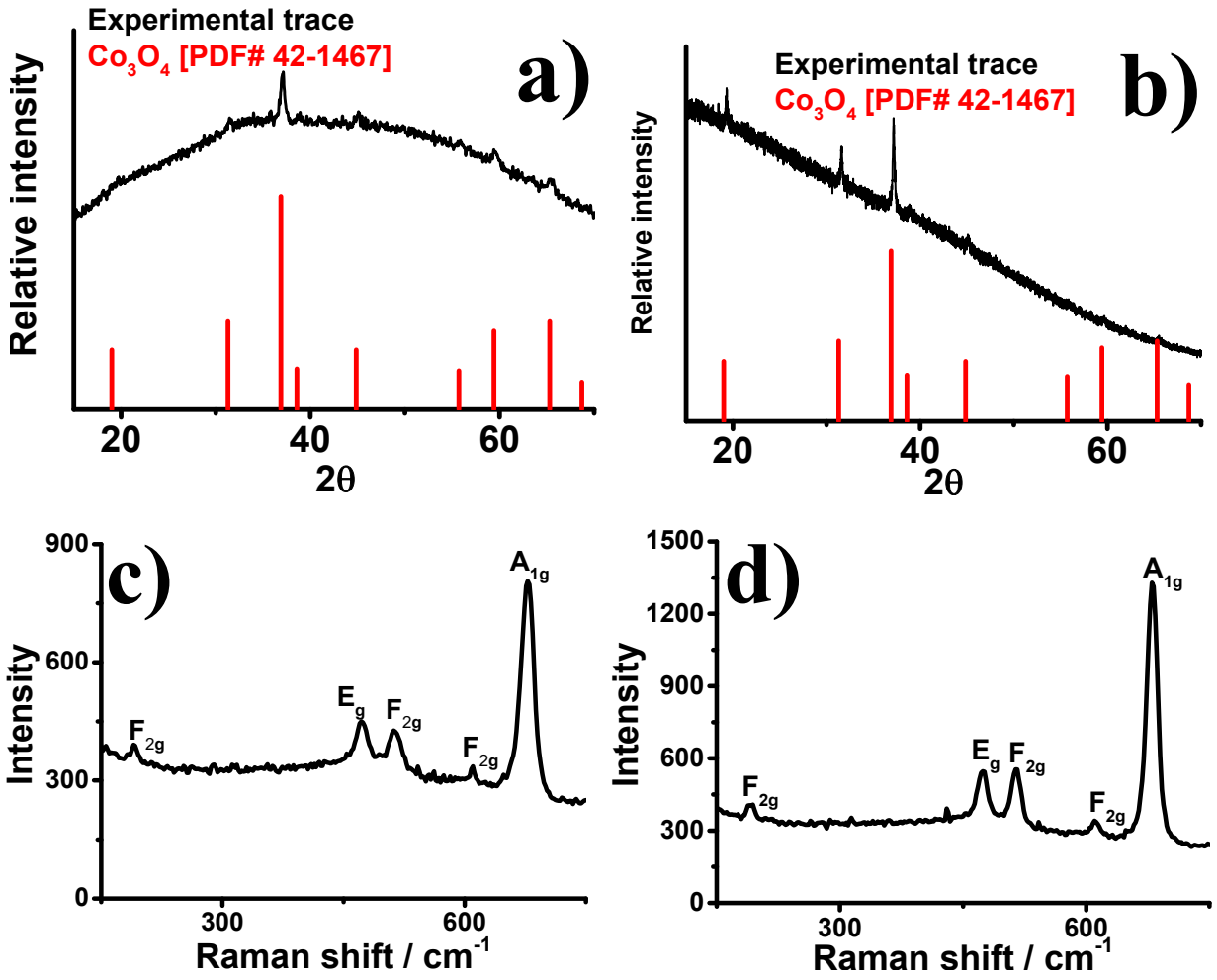

Fig. S17. XRD patterns and Raman spectra recorded after photocatalytic reaction of a), c) Co_3O_4-NPs and b), d) Co_3O_4-P-NS.

Appendix A. Calculation of the different concentration ratios of species in solution [25].

$$CO_2(aq) + H_2O \overset{K}{} H_2CO_3 \qquad K = \frac{[H_2CO_3]}{[CO_2(aq)]} \approx 0.002 \longrightarrow [CO_2] \approx 500 \bullet [H_2CO_3] \qquad \textbf{Eq. (A.1)}$$

$$pH = -\log [H^+] = 4.5\text{-}5 \longrightarrow [H^+] = 3.16\times10^{-5} - 1\times10^{-5} \qquad \textbf{Eq. (A.2)}$$

$$H_2CO_3 \overset{K_{a1}}{} HCO_3^- + H^+ \qquad K_{a1} = \frac{[HCO_3^-] \times [H^+]}{[H_2CO_3]} = 4.46 \times 10^{-7} \longrightarrow [H_2CO_3] \approx 71 - 23\,[HCO_3^-] \qquad \textbf{Eq. (A.3)}$$

References

[1] M. Rashad, M. Rüsing, G. Berth, K. Lischka, A. Pawlis, J. Nanomater. 2013 (2013) 714853.
[2] V.G. Hadjiev, M.N. Iliev, I.V. Vergilov, J. Phys. C Solid State 21 (1988) L199.
[3] C.W. Na, H.-S. Woo, H.-J. Kim, U. Jeong, J.-H. Chung, J.-H. Lee, CrystEngComm 14 (2012) 3737-3741.
[4] J. Xu, P. Gao, T.S. Zhao, Energy Environ. Sci. 5 (2012) 5333-5339.
[5] Z.P. Xu, H.C. Zeng, J. Mater. Chem. 8 (1998) 2499-2506.
[6] P. Lv, Y. Zhang, R. Xu, J.-C. Nie, L. He, J. App. Phys. 111 (2012) 013910.
[7] S.A. Makhlouf, J. Magn. Magn. Mater. 246 (2002) 184-190.
[8] Y. Ichiyanagi, S. Yamada, Polyhedron 24 (2005) 2813-2816.
[9] X.-P. Shen, H.-J. Miao, H. Zhao, Z. Xu, Appl. Phys. A 98 (2008) 47-51.
[10] S. Farhadi, J. Safabakhsh, P. Zaringhadam, J. NanoChem 3 (2013) 69.
[11] F. Cao, D. Wang, R. Deng, J. Tang, S. Song, Y. Lei, S. Wang, S. Su, X. Yang, H. Zhang, CrystEngComm 13 (2011) 2123-2129.
[12] S. Fan, Y. Zhang, X. Ma, E. Yan, X. Liu, S. Li, W. Liang, X. Zhai, Int. J. Electrochem. Sci. 8 (2013) 10498-10505.
[13] H. Yan, X. Xie, K. Liu, H. Cao, X. Zhang, Y. Luo, Powder Technol. 221 (2012) 199-202.
[14] K. Kaviyarasu, A. Raja, P.A. Devarajan, Spectrochim. Acta A 114 (2013) 586-591.
[15] L. Jin-bing, J. Zhi-quan, Q. Kun, H. Wei-xin, Chinese J. Chem. Phys. 25 (2012) 103-109.
[16] R. Berenguer, T. Valdés-Solís, A.B. Fuertes, C. Quijada, E. Morallón, J. Electrochem. Soc. 155 (2008) K110-K115.
[17] A. Younis, D. Chu, X. Lin, J. Lee, S. Li, Nanoscale Res. Lett. 8 (2013) 36.
[18] S.C. Petitto, M.A. Langell, J. Vac. Sci. Technol. A 22 (2004) 1690-1696.
[19] D. Barreca, A. Gasparotto, O.I. Lebedev, C. Maccato, A. Pozza, E. Tondello, S. Turner, G. Van Tendeloo, CrystEngComm 12 (2010) 2185-2197.
[20] G.S. Armatas, A.P. Katsoulidis, D.E. Petrakis, P.J. Pomonis, M.G. Kanatzidis, Chem. Mater. 22 (2010) 5739-5746.
[21] J. Feng, H.C. Zeng, J. Phys. Chem. B 109 (2005) 17113-17119.
[22] S.C. Petitto, E.M. Marsh, G.A. Carson, M.A. Langell, J. Mol. Catal. A-Chem. 281 (2008) 49-58.
[23] H.A.E. Hagelin-Weaver, G.B. Hoflund, D.M. Minahan, G.N. Salaita, Appl. Surf. Sci. 235 (2004) 420-448.
[24] Z. He, L. Wen, D. Wang, Y. Xue, Q. Lu, C. Wu, J. Chen, S. Song, Energy Fuels 28 (2014) 3982-3993.
[25] D.C. Harris, Quantitative Chemical Analysis, seventh ed., W.H. Freeman and Company, New York, 2007.